ROYAL SOCIETY
OF CHEMISTRY

PCCP

Maximizing NMR signal per unit time by facilitating fast *e-e-n* cross effect DNP

SCHOLARONE™
Manuscripts

Maximizing NMR signal per unit time by facilitating the e-e-n cross effect DNP rate

Alisa Leavesley,[1] Sheetal Jain,[1] Ilia Kamniker,[1] Hui Zhang,[2] Suchada Rajca,[2] Andrzej Rajca,[2*]
and Songi Han[1,3*]

[1] Department of Chemistry and Biochemistry, University of California, Santa Barbara, CA
[2] Department of Chemistry, University of Nebraska, Lincoln, NE
[3] Department of Chemical Engineering, University of California, Santa Barbara, CA
*Corresponding authors: songi@chem.ucsb.edu and arajca1@unl.edu

Abstract

The dynamic nuclear polarization (DNP) efficiency is critically dependent on the properties of the radical, solvent, and solute constituting the sample system. In this study, we focused on the three spin *e-e-n* cross effect (CE)'s influence on the nuclear longitudinal relaxation time constant T_{1n}, the build-up time constants of nuclear magnetic resonance (NMR) signal, T_{DNP} and DNP-enhancement of NMR signal. The dipolar interaction strength between the electron spins driving the *e-e-n* process was systematically modulated using mono-, di-, tri-, and dendritic-nitroxide radicals, while maintaining a constant global electron spin concentration of 10 mM. Experimental results showed that an increase in electron spin clustering led to an increased electron spin depolarization, as mapped by electron double resonance (ELDOR), and a dramatically shortened T_{1n} and T_{DNP} time constants under static and magic angle spinning (MAS) conditions. A theoretical analysis reveals that strong *e-e* interactions, caused by electron spin clustering, increase the CE rate. The three spin *e-e-n* CE is a hitherto little recognized mechanism for shortening T_{1n} and T_{DNP} in solid-state NMR experiments at cryogenic temperatures, and offers a design principle to enhance the effective CE DNP enhancement per unit time. Fast CE rates will benefit DNP at liquid helium temperatures, or at higher magnetic fields and pulsed DNP, where slow *e-e-n* polarization transfer rate is a key bottleneck to achieving maximal DNP performance.

Introduction

Dynamic nuclear polarization (DNP) is a powerful technique that enhances the nuclear magnetic resonance (NMR) signal intensities by several orders of magnitude. The improved sensitivity by DNP promises to transform the scope of solid state (ss) NMR towards achieving molecular imaging, surface characterization of materials and minute structural biology samples, previously inaccessible to NMR. In DNP, the NMR signal intensities are enhanced via the transfer of polarization from electron spins to the surrounding nuclear spins, facilitated by microwave (μw) irradiation. The source of electron spins for DNP is usually an extrinsic, paramagnetic, polarizing agent added to the sample in the form of a stable organic radical. The mechanism and efficiency of DNP depends on the electron and nuclear spin interactions, which are strongly modulated by the properties and concentration of the paramagnetic species. Notably, DNP has been successfully implemented for the study of solid interfaces to biological samples,[1–5] even in-cell systems[6–8] under both static and magic-angle-spinning (MAS) conditions, most commonly acquired around 90 K.[9–11] However, to fully establish DNP as a technique to predictably enhance the ssNMR performance, a better mechanistic understanding is needed of the DNP processes than currently available. Generally, maximizing the DNP performance implies maximizing the equilibrium DNP enhancement factor and minimizing the signal build-up time. In this study, we focus on the latter, specifically the spin dynamics that modulates the build-up time of NMR and DNP-NMR signal.

ss-DNP has two primary mechanisms: the solid effect (SE) and the cross effect (CE), where SE relies on a two-spin interaction (one electron and one nuclear spin)[12] and CE relies on three-spin interactions (two electron and one nuclear spins) to achieve polarization transfer from the electron spin(s) to the nuclear spin.[13] Direct μw irradiation on the forbidden transition between the electron and the hyperfine coupled nuclear spins results in SE DNP.[14] In contrast, CE DNP occurs when the Zeeman energies of two dipolar coupled electron spins differ by the Zeeman energy of a nuclear spin ($|v_{e1} - v_{e2}| = v_n$) that has unequal hyperfine couplings with the two CE-fulfilling electron spins.[15] The maximum polarization that can be transferred by the CE is determined by the polarization difference between the CE-fulfilling electron spins.[16–18] This polarization difference can be induced by direct μw irradiation on one of the electron spin populations, or may result from spectral diffusion via saturated electron spins that are not part of the CE-fulfilling electron spin pair—a mechanism also referred to as indirect CE.[19] The strength of the exchange and/or dipolar coupled electron-electron (*e-e*) network, which is tunable by the local radical concentration, can modulate the effective DNP mechanism between the SE and CE.[20–22] Another

classification of DNP is dissolution DNP (dDNP), where a static frozen sample is hyperpolarized at 0.8-5 K, and rapidly melted to carry out solution state NMR or magnetic resonance imaging (MRI) experiments at room temperature using the hyperpolarized sample. The thermal mixing (TM) mechanism is used primarily to rationalize dDNP processes that describe strongly coupled multi-electron and multi-nuclei spin systems utilizing a spin temperature formalism.[23,24] However, a fully quantum mechanics based theory of the DNP process of a multi-electron and multi-nuclei spin system, representative of a realistic sample, is lacking.[23]

The focus of DNP developments in recent years have been on the design and synthesis of efficient paramagnetic polarizing agents to reliably boost ss-DNP enhancement factors at high magnetic fields (B_0). As predicted by theory and verified experimentally, the SE and CE mechanisms become less effective at higher B_0.[25–27] Since the CE is more efficient at higher B_0 than SE, most DNP applications rely on the CE. To improve CE efficiency, designer bi-radicals have been synthesized with specific properties, such as long electron spin longitudinal relaxation time constants (T_{1e}), significant e-e couplings, and fixed electron spin g tensor orientations of tethered bi-radicals.[22,28–31] These designs generally focused on satisfying the CE condition by frequency matching, maximizing electron spin saturation via long T_{1e}, or more recently, reducing the depolarization induced by CE under MAS in the absence of µw irradiation. However, none of the existing DNP polarizing agents or methods are geared towards shortening the time constant for NMR and DNP signal build-up.

In this study, we thus focus on the understudied, yet critical, parameter to achieve optimal DNP performance, namely the effect the rate of polarization transfer from the electron spin(s) to the nuclear spins has on DNP. Detrimentally, the electron-nuclear (e-n) and electron-electron-nuclear (e-e-n) transfer rates for the SE and CE respectively are inversely proportional to B_0. Additionally, these polarization transfer rates must compete with the electron relaxation rates. Therefore, these combined effects can be key bottlenecks to achieving efficient e-n and e-e-n transfers under high B_0 and high temperature conditions. The polarization transfer rates are also crucial for pulsed DNP experiments, which are gaining interest due to the developing µw instrumentation, where optimum DNP is obtained with high power, but relatively short, µw pulses.[32–36]

The e-n and e-e-n transfer rates can influence, or even determine, the bulk nuclear polarization build-up time constant (T_{DNP}), which depends on a number of factors, including the underlying DNP mechanisms, the strength of the e-n interactions, and the external magnetic field strength that affects the polarization transfer rate, the electron spin relaxation rate, and the nuclear spin-diffusion rate.[37] In fact, many studies have utilized nuclear spin diffusion to enhance the polarization of nuclear spins located on interior surfaces of micro/nano-porous materials that the polarizing agents cannot physically reach given their bulky sizes. The DNP build-up curve has also been proposed as a method to characterize pore sizes.[38–40] For such studies to come to fruition, the contribution of the e-n and e-e-n transfer rates to T_{DNP} must be understood, and rendered negligible (i.e. fast), in order to reliably extract information on nuclear spin diffusion from the DNP build-up curves. Identifying the mechanisms to minimize T_{DNP} is especially relevant for dDNP, where signal build-up can take hours to maximally hyperpolarize a single sample for MRI studies,[41,42] for ss-DNP NMR imaging at liquid helium temperatures,[43] as well as for MAS-DNP under cryogenic temperatures, where the shot repetition time for signal averaging limits the acquisition rate.[44] To date, T_{DNP} has rarely been used as an explicit design parameter to optimize CE DNP. This can be attributed to an incomplete understanding of factors that tune e-n and e-e-n transfer rates and T_{DNP}.

The radical concentration also affects the nuclear spin relaxation times (T_{1n} and T_{2n}) via the paramagnetic relaxation enhancement (PRE) effects. The PRE effect on T_{1n} has been extensively studied and utilized in NMR to determine structural constrains.[45–47] However, the effect of multi electron spin interactions, such as that of the e-e interactions on T_{1n} is not known.[48] The existing PRE theories are valid under high temperature and low radical concentration conditions, where the e-n spin correlation time is very short and the effect of e-e interactions can be ignored.[49–51] Under such conditions, T_{1e} determines the correlation time of the local magnetic field fluctuations that governs the PRE effects on T_{1n}.[47] However, under DNP conditions both assumptions of short e-n correlation times and negligible e-e interactions are invalid, given the cryogenic temperatures and typically high radical concentrations employed for DNP. Recently, the effect of µw irradiation on the PRE effect has been demonstrated by Jain et al. under DNP conditions below 10 K;[52] however, the effect of e-e interactions on T_{1n} was not the focus of that study.[52] The effect of e-e coupling on T_{1n} has been observed in crystals of copper Tutton salts at temperature 1.4 K[53,54] and in frozen solutions of copper histidine at 5.5 K,[55] where T_{1n} was reduced with stronger e-e interactions in both cases. These two studies, however, proposed two different mechanisms for the reduction of T_{1n}, as will be discussed later.

In order to examine the role of *e-e* dipolar interactions on the *e-e-n* polarization transfer and electron and nuclear spin relaxation rates, we examined a series of radicals with a systematic increase in their *local* electron spin concentration (mono-radical, bi-radicals, tri-radical, and a dendrimer with 9 nitroxide moieties – shown in figure 1), while maintaining a constant global electron spin concentration of 10 mM. The active DNP mechanisms and DNP enhancement factor (ε) for these systems, along with their experimental electron spin (T_{1e} and T_M) and nuclear spin relaxation time constants were analyzed. The experimental results combined with a theoretical analysis of the CE DNP polarization transfer time (t_{een}) and the rate equations defining T_{DNP} demonstrated that the number and strength of the *e-e* dipolar interactions significantly shorten both T_{1n} and T_{DNP}, under static and MAS conditions. Electron-electron double resonance (ELDOR) experiments were used to directly measure the effect of these *e-e* dipolar coupled networks on the depolarization of the EPR spectrum when driven by μw irradiation. We found that the strength of the *e-e* dipolar coupled network correlates with the extent of electron spin depolarization, the CE efficiency, and the nuclear spin relaxation rates. The shortening of the nuclear spin relaxation rates can serve as a design criterion for choosing DNP radical/solvent system, where long T_{1n} and T_{DNP} are limiting factors at cryogenic temperatures and higher magnetic fields.
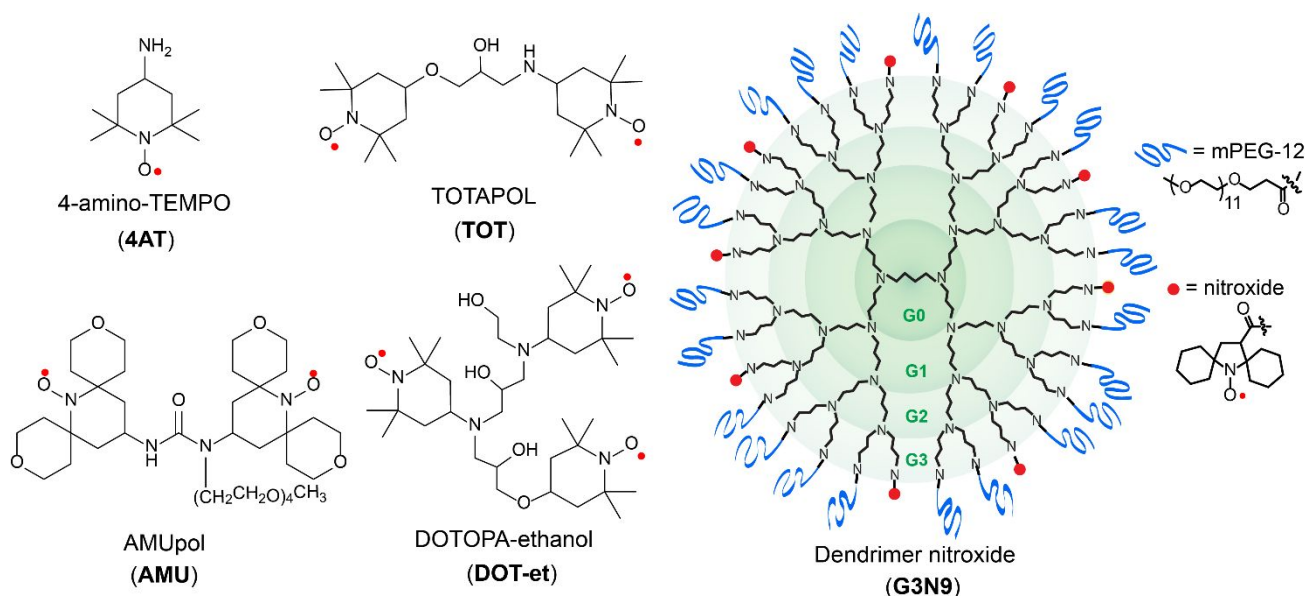

Figure 1. *The chemical structures of the mono-, bi-, and poly-radicals used in this study are shown. An average of 9 electron spins per dendrimer radical were considered based on end-group analyses.*

Materials and methods

4-amino-TEMPO (4AT, Sigma-Aldrich), TOTAPOL (TOT, DyNuPol), AMUpol (AMU, CortecNet), DOTOPA-ethanol (DOT-et, provided by Tycko), deuterium oxide (Cambridge Isotopes), and d8-glycerol (Cambridge Isotopes) were used as received. DOT-et was synthesized according to Yau et al and is a tri-radical,[56] and the G3N9 dendrimers[57] were synthesized according to the procedure in the electronic supplemental information (ESI) and scheme S1 and have an average of 9-electron spins per dendrimer according to end group analysis (ESI, figures S1-S3, and table S1). The structures for the radicals are shown in figure 1. Each nitroxide radical was dissolved in a stock solution of 6:3:1 by volume of d8-glycerol : D2O : H2O and diluted to 10 mM electron spins, where the radical concentrations of 4AT was 10 mM, TOT and AMU were 5 mM, DOT-et was 3.33 mM, and G3N9 was 1.11 mM. Water was purified with a μ-Pure water system (Pure Power, Korea; 12.5 MΩ) prior to use. 40 μL of sample was pipetted into a cylindrical Teflon sample holder (6 mm i.d. and 7 mm height with 1 mm wall thickness) and was cooled to 4 K by continuous helium flow.

The hardware for DNP and EPR based experiments have been previously described, where all static DNP, NMR, and EPR experiments were conducted at 7 T and at 4 K.[10] MAS-DNP experiments were conducted on a Bruker 400 MHz ASCEND DNP-NMR spectrometer for solids at 92 K. All static ^{1}H experiments were obtained with a saturation recovery pulse sequence followed by a 60 s delay and a solid echo detection (90x-t-90y), with the pulse sequence shown in the inset of figure 2b. MAS DNP experiments utilized a saturation recovery pulse sequence followed by a standard cross polarization from ^{1}H to ^{13}C. DNP enhancements are the NMR signal with

µw irradiation relative to the NMR signal without µw irradiation (S_{MWon}/S_{MWoff}). DNP profiles and power curves were obtained by measuring the DNP enhancement as a function of µw frequency ($\nu_{\mu w}$) and power ($P_{\mu w}$), respectively. The pulse sequence for acquiring electron spin relaxation measurements is shown in figure S4. Further descriptions of the hardware and experimental methods used for DNP and EPR can be found in the ESI.

Results/Discussion

As this study is focused on minimizing nuclear relaxation and polarization build-up time constants, we first recapitulate the relation between these time constants and the nuclear magnetization at any given time. Equations 1 and 2 determine the net magnetization in the $z-$ direction without and with µw irradiation, respectively.

$$M_{z,off}(t) = M_{z,off_{eq}}\left[1 - e^{-t/T_{1n}}\right] \tag{1}$$

$$M_{z,on}(t) = M_{z,on_{eq}}\left[1 - e^{-t/T_{DNP}}\right] \tag{2}$$

$M_{z,off_{eq}}$, $M_{z,on_{eq}}$, T_{1n}, and T_{DNP} are determined by fitting these equations to experimental data, where t is the build-up time ($t_{build-up}$) varied *without* or *with* µw irradiation. The initial magnetization at $t=0$ is assumed to be zero in both the cases as pre-saturation pulses were used in the measurements. The time constants T_{DNP} and T_{1n} are critical in determining the net NMR signal per unit time. The DNP signal enhancement at any time t, (ε_t) is determined by the signal ratio of µw on and off when recorded using the same build-up time or can be calculated using equation 3.

$$\varepsilon_t = \frac{M_{z,on}(t)}{M_{z,off}(t)} \tag{3}$$

$$\varepsilon_{eq} = \frac{M_{z,on_{eq}}}{M_{z,off_{eq}}} = \frac{M_{z,on}(t)}{M_{z,off}(t)}\frac{\left[1 - e^{-t/T_{1n}}\right]}{\left[1 - e^{-t/T_{DNP}}\right]}, \tag{4}$$

The equilibrium enhancement, ε_{eq}, was determined by fitting the T_{1n} and T_{DNP} models to the experimental data as shown by equation 4. Note ε_{eq} can be significantly different from ε_t at an arbitrary t depending on the difference in T_{1n} and T_{DNP} values.[36] $T_{1n} \geq T_{DNP}$, as will be discussed later, therefore, $\varepsilon_t \geq \varepsilon_{eq}$, where ε_t is significantly larger at short build-up times and approaches ε_{eq} as the build-up times lengthen. This is evident from figure S5 that illustrate the relationships of $M_{z,off}(t)$, $M_{z,on}(t)$, ε_t, and ε_{eq} for 10 mM 4AT.

To see the impact of local electron spin concentration on the two build-up rates, T_{1n} and T_{DNP}, and hence on the DNP enhancement, we performed experiments DNP experiments with 5 different radicals with varying number of electron spins per radical. A global electron spin concentration of 10 mM was chosen to limit the strength of the inter-radical interactions for the radical with the highest radical concentration, here the monoradical. The nitroxide-based radicals chosen for this study included a monoradical (10 mM 4-amino TEMPO (4AT)), a flexible and rigid bi-radical (5 mM TOTAPOL (TOT) and AMUpol (AMU), respectively), a tri-radical (3.33 mM DOTOPA-ethanol (DOT-et)), and a G3 dendrimer decorated with an average of 9 nitroxide moieties per macromolecule (1.1 mM G3N9), as depicted in figure 1.

In order to use the optimal DNP conditions to determine the T_{DNP}, which are critically dependent on the radical concentration and type as well as µw frequency and power, we begin by showcasing the enhancement factors dependence on µw frequency and power as shown in figure 2. The ε_t vs µw frequency ($\nu_{\mu w}$) curves, known as "DNP profiles" can be used to distinguish the active DNP mechanism(s) in the system. The $\nu_{\mu w}$ difference between positive and negative maxima (Δ_{DNP}) is less than $2\omega_n$ for CE DNP and equal to $2\omega_n$ for SE DNP.

Furthermore, in the case of CE, the whole profile falls within the range of the allowed EPR spectrum of the radical,[17,37,58] whereas it can extend beyond the allowed electron spectral density in SE DNP.[59–61] A system with both CE and SE contributions will display attributes of both mechanisms in the DNP profile lineshape.[21]

The DNP profiles for all the radicals are shown in figure 2a, which were measured with a $t_{build-up}$ of 60 s and optimum µw power ($P_{µw}$) as determined from the DNP power curves shown in figure 2b. The DNP profile of the mono-radical, 4AT, shows a Δ_{DNP} of 550 MHz, while the wings of the profile extended beyond the allowed EPR spectrum (black trace, figure 2a), which is a manifestation of mixed SE and CE contributions. This indicates that inter-radical interactions are present at 10 mM mono-radical, otherwise the mechanism would be purely SE. All the other radicals studied here display DNP profiles with primarily CE contributions: with a Δ_{DNP} of 450 MHz and the DNP profiles fitting within the range of the allowed EPR spectrum, as best seen in the normalized DNP profiles shown in figure S6, where further discussions of distinguishing the DNP mechanism from the DNP mechanism are presented in the ESI.
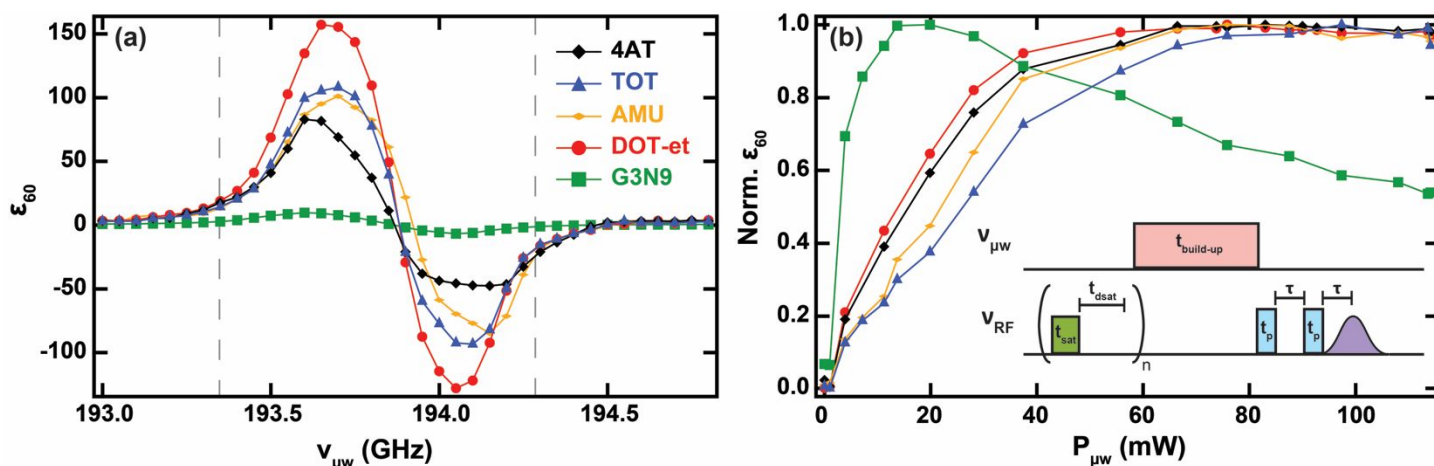

Figure 2. (a) DNP profiles at 4K and at 7 T for 10 mM 4AT (black diamond), 5 mM TOT (blue triangle), 5 mM AMU (yellow small diamond), 3.33 mM DOT-et (red circle), and 1.11 mM G3N9 (green square) in 6:3:1 d_8-glycerol:D_2O:H_2O. The dashed lines represent the width of the allowed EPR spectrum. (b)The normalized DNP power curves acquired with µw irradiation at 193.65 GHz. All data was acquired with a saturation recovery solid echo pulse sequence as shown in the inset of (b) with t_p = 2.5 µs, τ = 110 µs, t_{sat} = 2.4 µs, t_{dsat} = 380 µs, n = 10, and $t_{build-up}$ = 60 s.

The normalized DNP power curves in figure 2b were recorded using a $t_{build-up}$ of 60 s, ε_{60}, and $\nu_{µw}$ corresponding to the positive maximal condition from figure 2a. All DNP power curves reach a plateau at $P_{µw}$ ~65 mW of power, except for the dendrimer. Instead the maximum of ε_{60} occurs at $P_{µw}$ ~20 mW for the dendrimer, and the ε_{60} was reduced by 45% when irradiating with 120 mW instead of 20 mW. Such behavior is known as oversaturation, which has been observed for high global electron spin concentrations (>20 mM) at 4-6 K, and was hypothesized to result from electron spectral diffusion (eSD) achieving beyond optimal electron spin depolarization for CE DNP.[18,20] The manifestation of oversaturation with 10 mM of global electron spins indicates a strong eSD process that is driven by the dendritic intra-radical e-e interactions, as discussed later. These determined optimal $\nu_{µw}$ and $P_{µw}$ to achieve maximum positive DNP enhancement for each radical were then used to acquire the T_{DNP} data.

The T_{1n} and T_{DNP} values for the five radicals studied here are listed in table 1, and were found to decrease significantly from mono-, bi-, tri-radical to the dendrimer. Notably, the dendrimer has 37-fold and 60-fold smaller T_{1n} and T_{DNP} than the monomer, respectively (figure 3, raw data in figure S7) and both the values are an order of magnitude smaller than those of DOT-et. Interestingly, the bi-radicals (TOT and AMU) show distinctly different T_{1n} values (attributed to the difference in the rigidity of the molecular structures), whereas the T_{DNP} values are comparable for the two. The ε_{60} and ε_{eq} for the five radicals are also reported in table 1, and in general increase from mono- to tri-radical, but both decrease for the dendrimer. Under these experimental conditions, TOT has the lowest ε_{eq}. Besides the signal enhancement factors, an important practical figure of merit is the signal or signal to

noise (SNR) ratio per unit time that determines the experimental efficiency, which is proportional to $1/\sqrt{T_{DNP}}$ and $1/\sqrt{T_{1n}}$ for the µw on and off cases, respectively. Since a comparison of SNR for experimental data from different samples is difficult, we instead rely on the normalized signal per unit time at equilibrium, s_{eq}, as defined in equation 5.

$$s_{eq} = \left(\frac{M_{z,on_{eq}}}{\sqrt{T_{DNP}}}\right)\frac{1}{M_{z,off_{eq}}} = \frac{\varepsilon_{eq}}{\sqrt{T_{DNP}}} \qquad (5)$$

s_{eq} is proportional to the SNR normalized to the equilibrium magnetization without µw irradiation, as $M_{z,off_{eq}}$ should ideally be the same for fixed sample volumes and constant global electron spin concentrations. We found that s_{eq} increases with increasing local electron spin concentration, such that the dendrimer provides the largest s_{eq} owing to its extremely short T_{DNP} (Table 1). This implies that the dendrimer can outperform the other radicals by enabling fast signal averaging, as the repetition delay should be 5 times T_{DNP} to ensure full signal build-up— this will be explicitly demonstrated in the conclusion section (see ESI for additional discussion, figure S8). Care must be taken when comparing s_{eq} between different DNP systems, even between nominally comparable sample systems, because temperature, magnetic field, µw power, and nuclear spin relaxation rates can influence s_{eq}.

Table 1. *Signal enhancement, T_{DNP} and nuclear relaxation times for the different radicals with 10 mM global electron spin concentration in DNP juice at 7 T magnetic field and 4 K temperature.*

Sample	T_{1n} (s)*	T_{DNP} (s)	ε_{60}	ε_{eq}	s_{eq}
4AT	5987.0 ± 172	560.25 ± 10.1	83	10.7	0.45
TOT	4511.6 ± 67.8	287.95 ± 6.14	117	7.6	0.45
AMU	2951.1 ± 34.6	286.36 ± 2.78	105	10.9	0.64
DOT-et	3213.8 ± 129	153.41 ± 5.67	173	13.8	1.11
G3N9	106.26 ± 1.21	15.06 ± 0.23	17.7	8.7	2.24

*T_{1n} of solvent only is 9789.5 ± 367 s

These observations indicate that the time constants T_{1n} and T_{DNP} are shortened with increasing local electron spin concentrations – i.e. increasing *e-e* dipolar coupling, as shown in table 1 and figure 3. Given the constant global electron spin concentration, the trend in T_{1n} values cannot be explained by existing PRE theories as they do not consider the effect of the local electron spin concentrations or the *e-e* couplings.[49–51] This can be substantiated by checking the correlation between T_{1n} and electron relaxation times constants (the T_{1e} and electron spin phase memory time, T_M), which should relate to the correlation times that modulate the PRE effect. The measured T_{1e} and T_M values are given in table 2, and the raw data are shown in figure S9. In general, T_{1e} moderately increased, and T_M decreased with increasing local electron spin concentration, which is in agreement with previous studies.[62] The T_{1e} for AMU is longer than TOT or the tri-radical, likely due to the rigidity of AMU compared to the other radical systems, which is consistent with the shorter T_{1n} of AMU compared to TOT according to PRE effects. However, there is no obvious correlation between the electron and nuclear spin relaxation time constants, e.g. TOT has shorter T_{1e} and the longer T_M compared to both 4AT and AMU, yet the TOT T_{1n} is shorter than that of 4AT and longer than that of AMU. This indicates that the PRE effect alone cannot explain the observed trend of T_{1n} shortening with increasing local electron spin concentration. However, there are studies that suggest at low temperatures T_M, instead of T_{1e}, determines the *e-n* correlation time, and thus the PRE effect,[52,63] but no correlation was found between T_M and T_{1n}, as mentioned above. These results together suggest that incoherent *e-n* relaxation is *not* the dominating modulator of T_{1n} and T_{DNP}. We observe that the T_M values of the bi-, tri-, and dendritic radicals decrease with increasing local electron spin concentration, which agrees with literature, where T_M decreases with increasing local radical concentrations due to stronger *e-e* interactions at low temperatures.[62] The shorter T_M for the mono-radical is likely due to stronger inter-radical coupling.

Table 2. *Electron relaxation times and spectral diffusion rates for different radicals with 10 mM global electron spin concentration in DNP juice at 7 T magnetic field and 4 K temperature.*

Sample	T_{1e} (ms)	T_M (μs)	Λ^{eSD} (μs³)
4AT	94.2 ± 7.2	13.7 ± 0.3	10
TOT	86.0 ± 2.0	16.3 ± 0.7	25
AMU	138.5 ± 4.9	13.2 ± 0.3	25
DOT-et	88.6 ± 16.6	12.6 ± 0.2	50
G3N9	151.81 ± 7.5	7.2 ± 0.1	1400

Since the existing theories of PRE are not applicable, we postulate that the underlying DNP mechanism is sensitive to the local electron spin concentration resulting in the dramatic changes in both T_{DNP} and T_{1n} through coherent processes. The dominant DNP mechanism in the present cases is CE as verified by the DNP profiles, shown in figure 2, and discussed in ESI section 4. A significant contribution from the SE is observed only for the mono-radical sample. In CE DNP, the polarization difference of two electron spins that meet the CE condition is transferred to a hyperfine coupled nuclear spin with an *e-e-n* transfer time for optimal CE, t_{een}, as expressed in equation 6. We derived this equation from first principles using average Hamiltonian theory (AHT) for the CE, with the full derivation provided in the ESI, yielding:

$$t_{een} = \frac{2\pi\omega_{0I}}{(B_{e_1 n} - B_{e_2 n})(d + 2J)}.$$ (6)

This equation shows that the *e-e-n* polarization transfer time constant at the CE condition, t_{een}, depends on the nuclear Larmor frequency, ω_{0I}, the *e-e* interaction strengths including both dipolar coupling, d, and *J*-coupling, J, and the difference of the hyperfine couplings between each of the two electron spins and the nuclear spin, $\Delta B = B_{e_1 n} - B_{e_2 n}$. An analogous relationship was recently derived by Thankamony et al. using a different approach with a unitary transformation to diagonalize the electron spin Hamiltonian and obtain the transition moment for the *e-e-n* transition.[64] In the current analysis (presented in detail in the ESI), we have additionally explicitly derived a scaling factor for CE, $\kappa_{CE} = \Delta\Omega_S / \sqrt{(\Delta\Omega_S^2 + (d + 2J)^2)}$, that dictates the maximum possible transfer at a given field and *e-e* interaction strength (see the discussion after equation 21 in the ESI for more details). Here, $\Delta\Omega_S$ is the difference in the resonance frequencies of the participating electron spins. Interestingly, κ_{CE} decreases with stronger *e-e* interactions at any given field, and increases with increasing field strength in the presence of strong *e-e* coupling, or remains constant if *e-e* coupling is weak. This result is counter to the common belief that CE DNP enhancement should principally decrease with increasing field strength. However, the polarization transfer rate becomes faster with stronger *e-e* interaction strengths (shortening t_{een}) and significantly slows down at higher fields as shown in equation 6. This slow-down of the *e-e-n* transfer rate is the basis of the typically observed decrease in CE DNP enhancement with increasing magnetic fields. Thus, the main bottleneck of CE DNP is the competition between the *e-e-n* transfer rate and the electron spin relaxation rates. Therefore, fast *e-e-n* rates can be beneficial for achieving high performance CE DNP at high magnetic fields, where the electron spin relaxation rates become faster. We show that in the presence of multiple electron spin pairs fulfilling the CE condition, the *effective e-e-n* polarization transfer rate constant is the sum over all $1/t_{een}$ rates for the available *e-e-n* ensemble, culminating in k_{een}^{eff}, as expressed in the following equation (and derived in ESI equation 24), where $k_{ee_j n} = 1/t_{ee_j n}$:

$$k_{een}^{eff} = \sum_{j=1}^{N_{ee}} k_{ee_j n} = \frac{\Delta B(d + 2J)^{eff}}{2\pi\omega_{0I}}$$ (7)

As $(d + 2J)^{eff}$ is the cumulative coupling strength between all the *e-e* pairs, it increases with the number of *e-e* pairs satisfying the CE condition (N_{ee}) and/or the *e-e* coupling strength itself (as described below and in ESI section 8), hence the *e-e-n* transfer rate, k_{een}^{eff}, becomes faster. A faster *e-e-n* polarization transfer rate, k_{een}^{eff}, can

subsequently shorten T_{DNP}, which is modulated by both the *e-e-n* polarization transfer rate and the nuclear spin-diffusion rate, as long as the nuclear spin diffusion rate is not solely rate limiting, as will be discussed next.
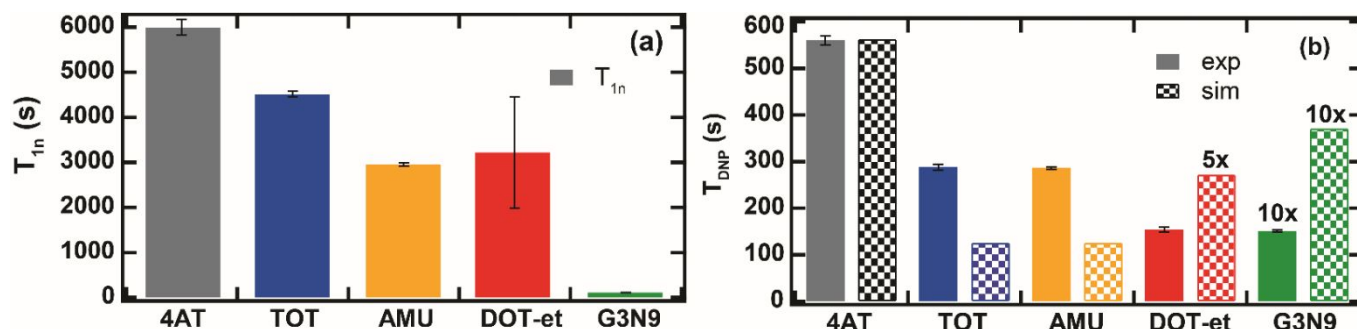

Figure 3. *Experimentally determined T_{1n} (a) and T_{DNP} (b-solid) for each radical. (b) A comparison of experimental (solid) and simulated (checkered) T_{DNP} for each case. The values for G3N9 in (b) are 10x to ease visualization, while those of the simulated DOT-et T_{DNP} are magnified 5x. Here the simulated T_{DNP} is extracted from the mono-exponential fit of the total nuclear spin polarization shown in figure S10, where $K_{sd} = 0.001$ Hz, $\Delta B = 1$ kHz, and the values of t_{een} are extracted from equation 7 for each radical. Further details of how t_{een} and T_{DNP} were calculated can be found in the ESI.*

The T_{DNP} is influenced by the *e-e-n* polarization transfer rate as well as the nuclear spin diffusion rate. If the two rates are significantly different, then the slower process determines the value of T_{DNP}. However, if these two rates are comparable, then both the *e-e-n* transfer rate and the nuclear spin diffusion rate will affect the T_{DNP}. To verify the hypothesis that the CE transfer rate is dictating the trend in T_{DNP} and T_{1n}, we simulated the T_{DNP} curves for the different radicals using a model system that represents a sample with N_{ee} number of *e-e* pairs at the CE condition coupled with N_n nuclear spins with different hyperfine coupling strengths. We used equation 7 to calculate the effective *e-e-n* transfer rate constant and incorporated a spin-diffusion rate constant K_{sd} in the differential equations describing nuclear and electron polarizations (see ESI section 9). The calculation of k_{een}^{eff} was performed in two steps: first, we calculated the effective *e-e* interaction strengths $(d + 2J)^{eff}$ and then calculated the hyperfine coupling difference, ΔB, using the model system comprising multiple electron and nuclear spins.

The effective *e-e* interaction strengths $(d + 2J)^{eff}$ were calculated by determining the cumulative dipolar coupling $(d = \mu_0 \gamma_{e1} \gamma_{e2}/4\pi r_{ee}^3)$ resulting from all the possible intra- and inter-radical *e-e* pairs when considering pairs of radicals, while the effect of J coupling was not considered here. To calculate the dipolar interaction strength, intra-radical *e-e* distances of $r_{ee} = 1.3$ nm were used for the bi- and tri- radicals. For the dendrimer, the intra-radical r_{ee} values were calculated based on the distances between 9 uniformly distributed electron spins on a sphere of radius 2 nm, with a distribution that maximizes the minimum distance between any pair of spins (according to the Tammes problem).[65–67] The calculated r_{ee} values are 2.31, 2.98, 3.46, 3.65, and 3.77 nm. Gratifyingly, DEER performed at Q-band and at 80 K, with data analyzed by denoising analyses relying on WavPDS and singular value decomposition as developed by Srivastava, Freed, and coworkers,[68,69] experimentally validated the Tammes distances, with the most prominent distance found at approximately 2.3 nm, together with distances identified around 2.8 nm and 3 − 4 nm. The DEER measurement and analysis are detailed further in section 10 and figure S11 of the ESI. Given the experimental validation, the calculated Tammes distances were used in the model to extract the weighted intra-dendrimer *e-e* distances. To determine the inter-radical *e-e* interaction strengths, the average intermolecular distance between two neighboring radicals (considering each radical concentration) was assumed to be the same distance between all inter-radical *e-e* pairs. This average intermolecular distance was set to be the peak distance from the intermolecular nearest neighbor radical distribution curves as shown in figure S12 in ESI section 10. The effective *e-e* interactions were then calculated by taking the sum of all the intra- and inter- radical *e-e* interactions, d, weighted by the total number of *e-e* pairs resulting between two radicals for each radical type.

Next, to calculate the ΔB, we assumed that the nuclear spins are located in six spheres of radii $r_{en} = (r, 4r, 8r, 12r, 16r, 20r)$ centered at a polarizing center representing all the coupled electron spin pairs in the system with the effective e-e coupling strength calculated by the aforementioned method, as illustrated in figure S10. Here r is the distance at which ΔB is 1 kHz for the given orientation angles of the e-n hyperfine interaction, which was chosen such that the mono-radical simulations were in agreement with the experimental results. The hyperfine coupling strengths and hence their difference, ΔB_{en_i}, were scaled by $1/r_{en_i}^3$, where r_{en_i} is the distance between the electron spin with the stronger hyperfine interaction and the ith nuclear spin. The effective e-e-n polarization transfer rate constant ($\overline{k}_{een_i}$) for each nuclear spin type was computed, using $\omega_{0I} = 294.026$ MHz, the e-e interaction strength $(d + 2J)^{eff}$ calculated as described above, and the scaled ΔB for all r_{en} values as expressed in equation 6.

Finally, the nuclear spin diffusion rate constant $K_{sd} = 0.005$ s^{-1} was used together with the $k_{een_i}^{eff}$ in the rate equations defining the electron and nuclear spin polarization to connect the nearest nuclear spins to each other. The K_{sd} was chosen to fit the experimentally observed mono-radical T_{DNP} values. No relaxation processes were considered in these rate equations because the electrons spins are at a quasi-steady state during DNP, and the nuclear relaxation time is too long to impact these processes considering that $T_{1n} \approx 10^4$ sec for the vitrified solvent system without any paramagnetic species. These rate equations were used to determine the nuclear spin polarization build-up as function of time (section 9 of ESI), and the value for T_{DNP} was then extracted via a mono-exponential fit to the computed nuclear spin polarization build-up curves, as illustrated in figure S10c. A more detailed description of the model system, derivation of the rate equations, and fits to simulated data is given in section 9 of the ESI.

These computed T_{DNP} values are compared to the experimental T_{DNP} values in figure 3b. For easy visualization, the calculated and experimental T_{DNP} values for the dendrimer sample are shown with a 10x magnification, and the calculated T_{DNP} for DOT-et with a 5x magnification. We note that a key assumption made in these calculations are that all possible e-e interactions fulfill the CE condition; therefore, the computed T_{DNP} values are underestimated for all radical systems. Despite these simplifications, there is remarkable agreement between the trends for the experimental and calculated T_{DNP} values. More realistic calculations of k_{een}^{eff} would require the consideration of many other factors: the entire g and A anisotropy of the nitroxide radicals and their powder averaging to properly account for the statistics of electron spin pairs meeting the CE condition, the full distribution of e-e interaction distances for both inter- and intra- radical interactions, and accounting for multi-spin and multi-radical interactions in a sample instead of considering only pairwise interacting electron spins and radicals. This is beyond the scope of this work and the existing literature. Albeit simple, this model calculation clearly demonstrates the conditions under which t_{een} is a dominant modulator of T_{DNP}, and these conditions match our experimental conditions well.

The shortening of T_{DNP} with increasing local electron spin concentration has been attributed to e-e-n processes; however, the question remains what induces the dramatic reduction of T_{1n} with increasing radical concentration. Interestingly, the trend of T_{1n} closely tracks that of T_{DNP}, as illustrated in figure 3b (solid), while the absolute values differ by an order of magnitude. We hence posit that the same e-e couplings that shorten T_{DNP} also shorten T_{1n} via the same e-e-n CE transitions, where the polarization flows from the bulk nuclear spins to the core nuclear spins located in proximity to the paramagnetic centers that are then rapidly relaxed by the e-e-n CE processes. The primary difference between T_{1n} and T_{DNP} is that T_{DNP} is driven by μw irradiation that generates a polarization difference between the electron spins that is then transferred to the nuclear spins. In the T_{1n} process no μw irradiation is applied, but the same e-e-n process modulates the nuclear spin polarization and enhances its relaxation rate to reach thermal equilibrium. Therefore, besides increasing the e-e interaction strength, increasing the number of pairs fulfilling the CE condition will also expedite the T_{1n} nuclear relaxation processes. We note that the effect of multi e-e interactions on T_{1n} has been observed and analyzed earlier by Houten et al. and Stoll et al., where the studies were performed at lower magnetic fields of 1.13 T and 3.34 T, respectively.[53–55] Houten et al. rationalized the shortening of T_{1n} as an enhanced cross-relaxation induced by dipolar coupled electron spins separated by ω_{0n} (i.e. CE condition), while Stoll et al. utilized a T_{1e}-driven mechanism to explain the shortening of T_{1n}. Our findings agree and expand upon those presented by Houten et al.[53,54]

Even under MAS conditions with 8 kHz sample spinning at 92 K, the dendrimer radical shortened both T_{1n} and T_{DNP} by more than 2-fold compared to AMU (the gold standard for MAS-DNP at ~100 K). Specifically, a T_{DNP} of 1.97±0.33 s was found with G3N9 and 4.02±0.35 s with AMU, while a T_{1n} of 2.12 ± 0.55 s was found

with G3N9 and 4.25 ± 0.46 s with AMU. This indicates that the reduction of nuclear relaxation rates via CE transitions is consistent, independent of whether static or MAS conditions apply, and over a wide range of temperatures. The MAS-DNP experiments were performed in a 9.4 T DNP system (Bruker Biospin) on a ^{13}C - glycine sample vitrified in DNP juice with either AMU or G3N9 at a 10 mM global electron spin concentration, (see figure S13). Details of the experimental parameters for the MAS-DNP measurements can be found in the ESI.

Although we have compelling arguments for the role of *e-e* dipolar coupling in modulating T_{DNP} and T_{1n}, it is desirable to experimentally and directly quantify the extent of the *e-e* interactions of the different radical systems. To do so, electron depolarization profiles were acquired by Electron-eLectron DOuble Resonance (ELDOR), a pump-probe experiment, where the detection frequency (ν_{detect}) was held constant, and the excitation frequency (ν_{excite}) was stepped across the EPR spectrum.[19,70] In ELDOR, a hole is burnt into the EPR spectrum, the depth of which is influenced by the combined effects of T_{1e}, electron spectral diffusion (eSD), and $P_{\mu w}$,[70] and the width determined primarily by eSD and the μw irradiation bandwidth.[18] Here, eSD is a process facilitated by *e-e* interactions, where polarization is transferred between dipolar coupled electron spins at different resonant frequencies.

The ELDOR profiles for each radical system are shown in figure 4, where four ν_{detect} frequencies were chosen to sample the eSD effect across the EPR spectrum (the ELDOR pulse sequence is shown in the inset of figure 4d). With increased local electron spin concentration, the depth and width of the ELDOR profile increased, to the point where the dendrimer showed depolarization even beyond that of its allowed EPR spectral density (figure S14). The mono-radical, and to some extent the bi-radicals, do not display significant eSD, as found by limited depolarization in the center of the ELDOR spectrum. The ELDOR profiles of 4AT and TOT revealed forbidden transitions due to *e-n* hyperfine interactions (i.e. SE for each nuclear spin hyperfine coupled to the electron spin) as sharp symmetric peaks positioned the nuclear Larmor frequency away from the allowed EPR transition ($\nu_{detect}=\nu_{excite}$, annotated as peak 1 in figure 4c). The hyperfine coupled peaks for ^{14}N, ^2H, and ^1H forbidden transitions are identified in figure 4c as 2, 3, and 4, respectively. It is only with ≥ 3 coupled electron spins per radical that consistently large eSD effects were evident in the ELDOR profiles at all ν_{detect}. Simulations of these profiles that account for differences in electron and nuclear relaxation rates can extract a phenomenological eSD parameter (Λ^{eSD}), following the theory and simulation method described by Shimon et al.[21,71] These extracted Λ^{eSD} are listed in table 2. A comparison of the simulations and experimental ELDOR profiles are presented in figure S15, where good agreement was generally observed, with the relevant simulation parameters discussed in the ESI and reported in table S2. The Λ^{eSD} determined from simulations increased with the increased number of electron spins per radical, where both rigid and flexible biradicals yielded the same Λ^{eSD}. Therefore, we can conclude that eSD, as reflected in Λ^{eSD}, increases with local electron spin concentration, independent of T_{1e}. The presence of strong eSD provides direct evidence for a strongly coupled electron spin network. This enhances the *e-e-n* polarization transfer rate (i.e. CE efficiency), as indicated by equation (6) and reflected in the broad depolarization of the electron spins that generate polarization differences between coupled pairs of electron spins, resulting in shorter T_{DNP} and T_{1n} values. This is especially noteworthy for the two bi-radicals, AMU and TOT, as they have nearly identical Λ^{eSD} (Table 2) and T_{DNP} (Table 1) under μw irradiation. The ELDOR profiles also explain why the ε_{eq} of the dendrimer system is so low—the electron spin population across the whole EPR spectrum is nearly completely depolarized by strong eSD, where the lack of a polarization differential between the dipolar coupled electron spins limits the net transfer of polarization from the electron spins to the nuclear spins.
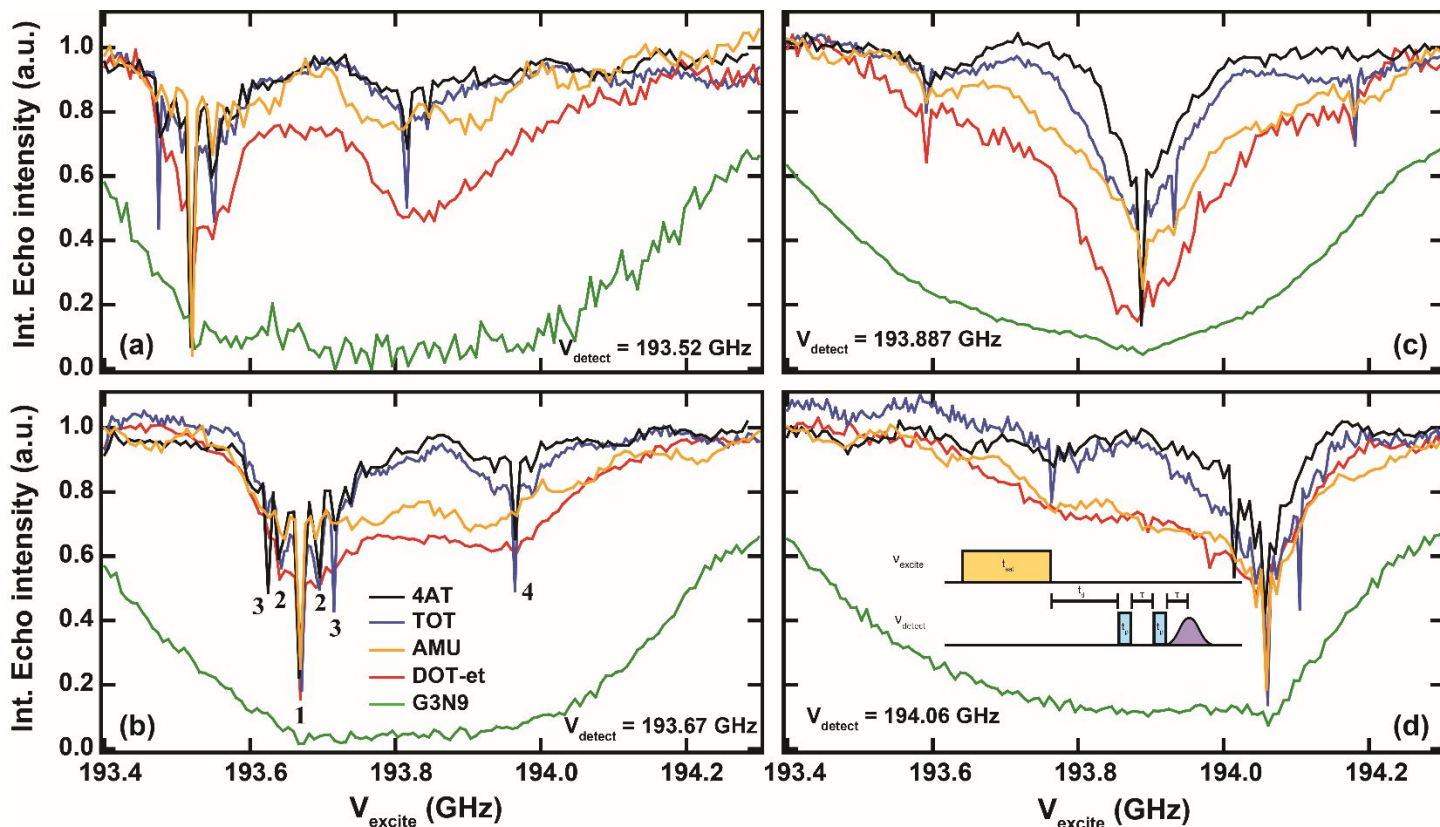
Figure 4. *Electron spin depolarization profiles measured via ELDOR at 4K with V_{detect} of 193.52 GHz (a), 193.67 GHz (b), 193.887 GHz (c), and 194.06 GHz (d) for 10 mM 4AT (black), 5 mM TOT (blue), 5 mM AMU (purple), 3.33 mM DOT-et (red), and 10 mM electron spin dendrimer G3N9 (green) in 6:3:1 d_8-glycerol:D_2O:H_2O. Allowed EPR transitions are denoted by 1, while 2, 3, and 4 denote the forbidden ^{14}N, ^2H, and ^1H transition, respectively. The ELDOR pulse sequence is shown as an insert in (d), where t_{sat} = 100 ms, t_p = 750 ns, t_d = 10 μs, and τ = 500 ns, with a recycle delay of 600 ms.*

If we consider the system with the strongest *e-e* dipolar coupled network, the dendritic G3N9 radical with 10 mM electron spin concentration revealed three outlying results: the power curve displaying DNP oversaturation (figure 2b), short T_{DNP} (figure 3b), and extensive electron spin depolarization according to the ELDOR profiles (figure 4). Before we look closer at these three results, we confirm that the CE in the dendritic radical arise from intra-radical interactions. A 1.7 mM electron spin concentration of G3N9 was used to confirm that only the CE DNP mechanism is active via a DNP profile analysis (figure S16). As the intra-radical distance for 1.7 mM electron spin dendrimer is > 11 nm on average, the observed CE DNP must solely originate from the intra-radical *e-e* dipolar couplings within a *single* dendritic G3N9 radical. This, in fact is largely confirmed experimentally by the DEER derived electron spin distance distribution, $P(r)$, in G3N9, which is similar at electron spin concentrations of 1.7 and 10 mM (see figure S11). The full relaxation and enhancement values for the 1.7 mM and 10 mM electron spin G3N9 are shown in table S3. While we proposed in prior studies that DNP oversaturation is caused by broad depolarization across the EPR spectrum, measurement of power dependent electron spin depolarization profiles were not available at the time.[20] We confirm experimentally with ELDOR profiles measured as a function of $P_{μw}$, for the first time, that the DNP oversaturation observed at higher $P_{μw}$ originates from beyond-optimal electron spin depolarization for CE DNP as shown in figure 5a. Under oversaturation conditions, the effective polarization differentials between the electron spins meeting the CE condition were reduced; therefore, the CE polarization potential to polarize hyperfine coupled nuclear spins is also reduced. The exceptionally large eSD found for the dendrimer sample can explain why only the dendrimer sample exhibited DNP oversaturation at a global electron spin concentration of 10 mM.

Finally, T_{DNP} as a function of $P_{μw}$ was measured, and shown in figure 5b. The observed shortening of T_{DNP} with increasing $P_{μw}$ is due to an increase in the cumulative *e-e-n* polarization transfer rate. This rate increases with $P_{μw}$ due to an increase in the number of *e-e* pairs participating in CE, as verified by the ELDOR profiles. In the

ELDOR profiles broader electron spin depolarization indicates that more frequency sets of *e-e* pairs can participate in CE DNP, while the deeper depolarization indicates that more *e-e* pairs can participate at a single frequency set given the equalization of spin states. It should be noted that if the $P_{\mu w}$ increases sufficiently to saturate the electron spins such that the polarization difference between the participating pair of electron spins (ΔP_{ee}) reduces, then T_{DNP} will be shorter, but also the net transferred polarization lower, resulting in the oversaturation effect.
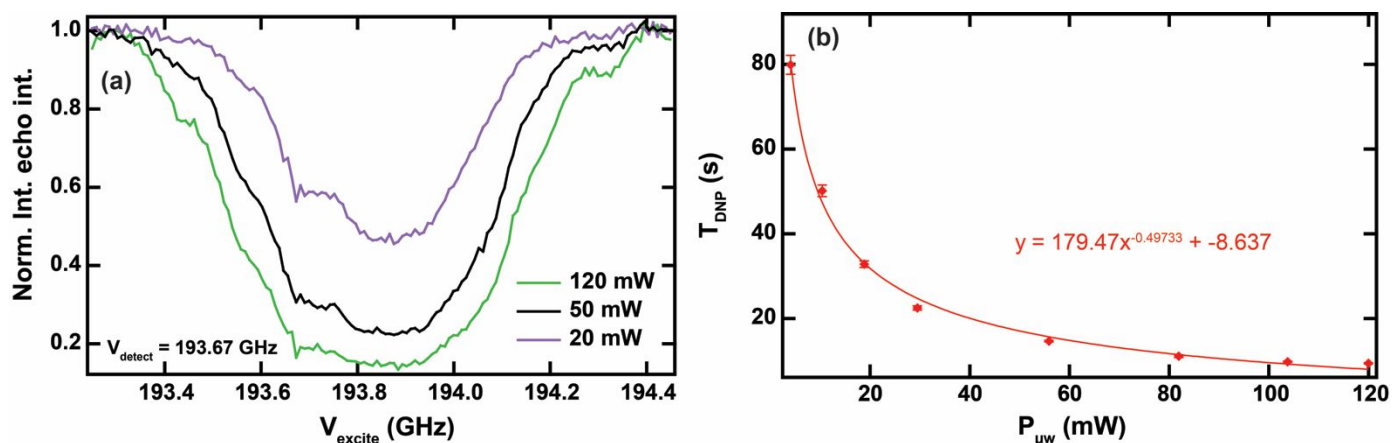
Figure 5. (a) Electron depolarization profiles of the 10 mM electron spin sample at different $P_{\mu w}$ for the saturation pulse: 120 mW (Oversaturation regime, green), 20 mW (Maximum DNP enhancement, black), and 5 mW (Equivalent enhancement as 120 mW, red). In the ELDOR pulse sequence, ν_{detect} = 193.67 GHz, t_{sat} = 100 ms, t_p = 750 ns, t_d = 10 μs, and τ = 500 ns, with a recycle delay of 600 ms and (b) DNP power dependent T_{DNP} for 10 mM electron spin of G3N9 in 6:3:1 d_8-glycerol:D_2O:H_2O at 4 K and at 7 T when irradiated with 193.65 GHz. T_{DNP} was determined at each $P_{\mu w}$ by fitting experimental results to $M_z(t) = M_{z_{eq}}\left(1 - e^{\frac{-t}{T_{DNP}}}\right)$, with the resultant fitting error shown in the figure.

Conclusion

This study provides design rules for DNP polarizing agents, which facilitate fast NMR signal build-up rates in presence and absence of μw irradiation based on a mechanistic understanding of the process involved. Higher local electron spin concentrations induced by either radical clustering or achieved with designer multi-electron spin radicals lead to an increased probability of *e-e-n* transitions that meet the CE condition. The increased *e-e-n* polarization transfer rates lead to shorter T_{DNP} under the experimental conditions presented here, demonstrating that the *e-e-n* polarization transfer rates are smaller or comparable to the nuclear spin diffusion rates. These same *e-e-n* transitions also caused fast relaxation of core nuclear spins that are connected to the bulk nuclear spins via spin-diffusion, and hence shortened the T_{1n}. The shortening of T_{1n} and T_{DNP} are observed under both static and MAS DNP conditions. This effect can be used to optimize the equilibrium DNP signal per unit time, s_{eq}, by shortening T_{DNP}—a hitherto underutilized tuning parameter for CE DNP. Choosing conditions and radical systems that yield a fast *e-e-n* transfer is particularly advantageous for CE DNP at high magnetic fields, where the *e-e-n* transfer rates become slower with higher nuclear Larmor frequency, whereas the competing electron spin relaxation rates become faster. The CE DNP efficiency at high magnetic fields can be maximized with (i) high populations of *e-e* pairs fulfilling the CE condition, and (ii) rapid *e-e-n* transfer rates. The problem of fewer *e-e* pairs fulfilling the CE conditions at high magnetic fields that have a net polarization differential can be solved by using shaped broad band pulse trains for continuous μw irradiation,[18] or short, high-powered μw pulses for broad EPR depolarization in driven processes, such as pulsed DNP.[72] This study shows that rapid *e-e-n* transfer rates can be designed by choosing DNP polarizing agents with clustered radicals. Fast *e-e-n* transfer is also paramount to achieve coherent transfer for pulsed DNP. Interestingly, high $P_{\mu w}$ shortened T_{DNP}, independent of whether DNP oversaturation occurred or not, which is rationalized by the increased electron spin depolarization that increases the population of excited electron spins that will relax to their ground state with higher $P_{\mu w}$, as revealed by the ELDOR profiles.

The effect of T_{DNP} on the accumulated NMR signal, amplified by DNP, can be effectively illustrated by simulating the effects of signal averaging for a total NMR acquisition time of 1 hour based on the measured T_{DNP} and ε_{eq} of the G3N9 dendrimer compared to the other radical systems studied here. The benefit of short T_{DNP} with increasing shot repetition time is illustrated in figure 6 (see ESI section 6 for more details and examples). We find that the dendritic G3N9 yields the largest NMR signals for shot repetition delays $< 10*T_{DNP}$, where it can clearly be seen that G3N9 outperforms its counterparts at low shot repetition delays. We conclude that shortening T_{DNP} by increasing the local electron spin concentration is a promising avenue to maximize the recorded NMR signal.
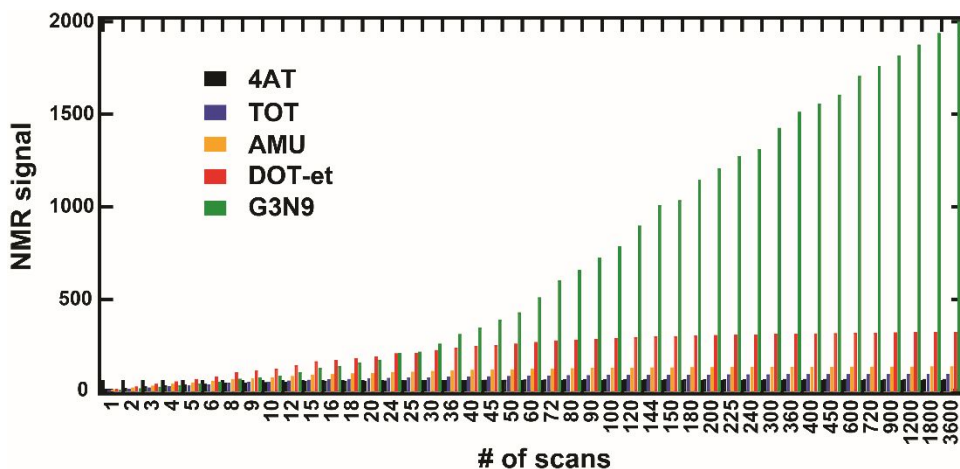

Figure 6. Simulated NMR signal ($M_{z,on}(t)$) after signal averaging for a total timeframe of 3600 sec, where the $t_{build-up}$*number of scans = total timeframe. Equation 2 was used and for this simulation with each radical's respective ε_{eq} and T_{DNP}, where $M_{z,on}(t)$*number of scans produced the reported NMR signal.

This study also points out that the polarization efficiency of nuclear spins tens to hundreds of nm away from the polarizing agent can result from a combination of direct e-e-n polarization transfer and nuclear spin diffusion processes, in which the direct transfer to nuclear spins further away from the polarizing agent can be a significant path if the polarizing agent has efficient e-e-n transfer rates. A full understanding of the polarization build-up process is necessary for quantitative studies that extract information about domain sizes, and surface morphology from the polarizing agent based on the shape and time constants of DNP build-up curves, or enable the polarization of remote nuclei.[38–40]

Finally, this study provided the first direct experimental evidence by ELDOR that DNP oversaturation is due to electron spin depolarization beyond optimal conditions with the dendrimer sample. This is attributed to the presence of strong e-e dipolar couplings that resulted in extensive eSD, where effective eSD was not observed for the mono- or bi-radicals at a global electron spin concentration of 10 mM.

In summary, from the experimental observations and theoretical analysis made in this study, it is evident that the e-e interaction strength and the number of e-e interactions should be a design criterion for the next generation radicals for DNP applications at high magnetic fields to tune the e-e-n polarization transfer rate and the value of and mechanism underlying T_{DNP}. Given that the overall performance of DNP is dictated by the amplified signal per unit time, shortening T_{DNP} is an effective, yet hitherto underutilized, approach to enhance the impact and broaden the scope of DNP enhanced NMR spectroscopy to imaging.

References

1   C. Bonhomme, C. Gervais and D. Laurencin, *Prog. Nucl. Magn. Reson. Spectrosc.*, 2014, **77**, 1–48.

2   A. M. Namespetra, D. A. Hirsh, M. P. Hildebrand, A. R. Sandre, H. Hamaed, J. M. Rawson and R. W. Schurko, *CrystEngComm*, 2016, **18**, 6213–6232.

3   Ü. Akbey, B. Altin, A. Linden, S. Özçelik, M. Gradzielski and H. Oschkinat, *Phys. Chem. Chem. Phys.*, 2013, **15**, 20706–16.

4   A. C. Pinon, J. Schlagnitweit, P. Berruyer, A. J. Rossini, M. Lelli, E. Socie, M. Tang, T. Pham, A. Lesage, S. Schantz and L. Emsley, *J. Phys. Chem. C*, 2017, **121**, 15993–16005.

5   T. Prisner and W. Köckenberger, *Appl. Magn. Reson.*, 2008, **34**, 213–218.

6   M. Renault, S. Pawsey, M. P. Bos, E. J. Koers, D. Nand, R. Tommassen-van Boxtel, M. Rosay, J. Tommassen, W. E. Maas and M. Baldus, *Angew. Chemie Int. Ed.*, 2012, **51**, 2998–3001.

7   K. K. Frederick, V. K. Michaelis, B. Corzilius, T. Ong, A. C. Jacavone, R. G. Griffin and S. Lindquist, *Cell*, 2015, **163**, 620–628.

8   T. Viennet, A. Viegas, A. Kuepper, S. Arens, V. Gelev, O. Petrov, T. N. Grossmann, H. Heise and M. Etzkorn, *Angew. Chemie - Int. Ed.*, 2016, **55**, 10746–10750.

9   D. Lee, E. Bouleau, P. Saint-Bonnet, S. Hediger and G. De Paëpe, *J. Magn. Reson.*, 2016, **264**, 116–124.

10 T. A. Siaw, A. Leavesley, A. Lund, I. Kaminker and S. Han, *J. Magn. Reson.*, 2016, **264**, 131–153.

11 M. Rosay, L. Tometich, S. Pawsey, R. Bader, R. Schauwecker, M. Blank, P. M. Borchard, S. R. Cauffman, K. L. Felch, R. T. Weber, R. J. Temkin, R. G. Griffin and W. E. Maas, *Phys. Chem. Chem. Phys.*, 2010, **12**, 5850–5860.

12 Y. Hovav, A. Feintuch and S. Vega, *J. Magn. Reson.*, 2010, **207**, 176–189.

13 Y. Hovav, A. Feintuch and S. Vega, *J. Magn. Reson.*, 2012, **214**, 29–41.

14 A. A. Smith, B. Corzilius, A. B. Barnes, T. Maly and R. G. Griffin, *J. Chem. Phys.*, 2012, **136**, 015101.

15 D. Banerjee, D. Shimon, A. Feintuch, S. Vega and D. Goldfarb, *J. Magn. Reson.*, 2013, **230**, 212–219.

16 C. F. Hwang and D. A. Hill, *Phys. Rev. Lett.*, 1967, **19**, 1011–1014.

17 W. T. Wenckebach, *J. Magn. Reson.*, 2017, **284**, 104–114.

18 I. Kaminker and S. Han, *J. Phys. Chem. Lett.*, 2018, **9**, 3110–3115.

19 Y. Hovav, D. Shimon, I. Kaminker, A. Feintuch, D. Goldfarb and S. Vega, *Phys. Chem. Chem. Phys.*, 2015, **17**, 6053–6065.

20 T. A. Siaw, M. Fehr, A. Lund, A. Latimer, S. A. Walker, D. T. Edwards and S. Han, *Phys. Chem. Chem. Phys.*, 2014, **16**, 18694–18706.

21 A. Leavesley, D. Shimon, T. A. Siaw, A. Feintuch, D. Goldfarb, S. Vega, I. Kaminker and S. Han, *Phys. Chem. Chem. Phys.*, 2017, **19**, 3596–3605.

22 G. Mathies, M. A. Caporini, V. K. Michaelis, Y. Liu, K. Hu, D. Mance, J. L. Zweier, M. Rosay, M. Baldus and R. G. Griffin, *Angew. Chemie - Int. Ed.*, 2015, **54**, 11770–11774.

23 W. T. Wenckebach, *J. Magn. Reson.*, 2017, **277**, 68–78.

24 S. C. Serra, A. Rosso and F. Tedoldi, *Phys. Chem. Chem. Phys.*, 2012, **14**, 13299–13308.

25 K.-N. Hu, G. T. Debelouchina, A. A. Smith and R. G. Griffin, *J. Chem. Phys.*, 2011, **134**, 125105-125105–19.

26 D. Banerjee, D. Shimon, A. Feintuch, S. Vega and D. Goldfarb, *J. Magn. Reson.*, 2013, **230**, 212–219.

27 K. R. Thurber and R. Tycko, *Isr. J. Chem.*, 2014, **54**, 39–46.

28 D. J. Kubicki, G. Casano, M. Schwarzwälder, S. Abel, C. Sauvée, K. Ganesan, M. Yulikov, A. J. Rossini, G. Jeschke, C. Copéret, A. Lesage, P. Tordo, O. Ouari and L. Emsley, *Chem. Sci.*, 2016, **7**, 550–558.

29 A. Zagdoun, G. Casano, O. Ouari, M. Schwarzwälder, A. J. Rossini, F. Aussenac, M. Yulikov, G. Jeschke, C. Coperet, A. Lesage, P. Tordo and L. Emsley, *J. Am. Chem. Soc.*, 2013, **135**, 12790–12797.

30 C. Sauvée, M. Rosay, G. Casano, F. Aussenac, R. T. Weber, O. Ouari and P. Tordo, *Angew. Chemie - Int. Ed.*, 2013, **52**, 10858–10861.

31 C. Sauvée, G. Casano, S. Abel, A. Rockenbauer, D. Akhmetzyanov, H. Karoui, D. Siri, F. Aussenac, W. Maas, R. T. Weber, T. Prisner, M. Rosay, P. Tordo and O. Ouari, *Chem. - A Eur. J.*, 2016, **22**, 5598–5606.

32   G. Mathies, M. A. Caporini, V. K. Michaelis, Y. Liu, K. N. Hu, D. Mance, J. L. Zweier, M. Rosay, M. Baldus and R. G. Griffin, *Angew. Chemie - Int. Ed.*, 2015, **54**, 11770–11774.

33   S. K. Jain, G. Mathies and R. G. Griffin, *J. Chem. Phys.*, 2017, **147**, 164201.

34   T. V. Can, J. J. Walish, T. M. Swager and R. G. Griffin, *J. Chem. Phys.*, 2015, **143**, 054201.

35   T. Van Can, J. E. McKay, R. T. Weber, C. Yang, T. Dubroca, J. Van Tol, S. Hill and R. G. Griffin J Phys Chem Lett, *J. Phys. Chem. Lett.*, 2018, **9**, 3187–3192.

36   G. Mathies, S. Jain, M. Reese and R. G. Griffin, *J. Phys. Chem. Lett.*, 2016, **7**, 111–116.

37   Y. Hovav, A. Feintuch and S. Vega, *J. Chem. Phys.*, 2011, **134**, 074509.

38   E. Pump, J. Viger-Gravel, E. Abou-Hamad, M. K. Samantaray, B. Hamzaoui, A. Gurinov, D. H. Anjum, D. Gajan, A. Lesage, A. Bendjeriou-Sedjerari, L. Emsley and J.-M. Basset, *Chem. Sci.*, 2017, **8**, 284–290.

39   O. Lafon, A. S. L. Thankamony, T. Kobayashi, D. Carnevale, V. Vitzthum, I. I. Slowing, K. Kandel, H. Vezin, J. P. Amoureux, G. Bodenhausen and M. Pruski, *J. Phys. Chem. C*, 2013, **117**, 1375–1382.

40   A. J. Rossini, A. Zagdoun, F. Hegner, M. S. Der, D. Gajan, C. Coperet, A. Lesage and L. Emsley, *J. Am. Chem. Soc.*, 2012, **134**, 16899–16908.

41   J. H. Ardenkjaer-Larsen, A. M. Leach, N. Clarke, J. Urbahn, D. Anderson and T. W. Skloss, *NMR Biomed.*, 2011, **24**, 927–932.

42   S. Reynolds and H. Patel, *Appl. Magn. Reson.*, 2008, **34**, 495–508.

43   K. R. Thurber and R. Tycko, *Phys. Chem. Chem. Phys.*, 2010, **12**, 5779–5785.

44   A. B. Barnes, B. Corzilius, M. L. Mak-Jurkauskas, L. B. Andreas, V. S. Bajaj, Y. Matsuki, M. L. Belenky, J. Lugtenburg, J. R. Sirigiri, R. J. Temkin, J. Herzfeld and R. G. Griffin, *Phys. Chem. Chem. Phys.*, 2010, **12**, 5861–5867.

45   J. Clore, G. Marius; Iwahara, *Chem. Rev.*, 2009, **109**, 4108–4139.

46   J. Iwahara, C. D. Schwieters and G. M. Clore, *J. Am. Chem. Soc.*, 2004, **126**, 5879–5896.

47   C. P. Jaroniec, *J. Magn. Reson.*, 2015, **253**, 50–59.

48   F. X. Theillet, A. Binolfi, S. Liokatis, S. Verzini and P. Selenko, *J. Biomol. NMR*, 2011, **51**, 487–495.

49   I. Solomon, *Phys. Rev.*, 1955, **99**, 559–565.

50   W. E. Blumberg, *Phys. Rev.*, 1960, **119**, 79–84.

51   N. Bloembergen, E. M. Purcell and R. V Pound, *Phys. Rev.*, 1948, 679–746.

52   S. K. Jain, T. A. Siaw, A. Equbal, C. B. Wilson, I. Kaminker and S. Han, *J. Phys. Chem. C*, 2018, **122**, 5578–5589.

53   J. Van Houten, W. T. Wenckebach and N. J. Poulis, *Physica*, 1977, **92B**, 201–209.

54   J. Van Houten, W. T. Wenckebach and N. J. Poulis, *Physica*, 1977, **92B**, 210–220.

55   S. Stoll, B. Epel, S. Vega and D. Goldfarb, *J. Chem. Phys.*, 2007, **127**, 164511.

56   W. M. Yau, K. R. Thurber and R. Tycko, *J. Magn. Reson.*, 2014, **244**, 98–106.

57   A. Rajca, Y. Wang, M. Boska, J. T. Paletta, A. Olankitwanit, M. A. Swanson, D. G. Mitchell, S. S. Eaton, G. R. Eaton and S. Rajca, *J. Am. Chem. Soc.*, 2012, **134**, 15724–15727.

58   D. Shimon, Y. Hovav, A. Feintuch, D. Goldfarb and S. Vega, *Phys. Chem. Chem. Phys.*, 2012, **14**, 5729–5743.

59   D. Wiśniewski, A. Karabanov, I. Lesanovsky and W. Köckenberger, *J. Magn. Reson.*, 2016, **264**, 30–38.

60   Y. Hovav, O. Levinkron, A. Feintuch and S. Vega, *Appl. Magn. Reson.*, 2012, **43**, 21–41.

61   B. Corzilius, *Phys. Chem. Chem. Phys.*, 2016, **18**, 27190–27204.

62   D. T. Edwards, S. Takahashi, M. S. Sherwin and S. Han, *J. Magn. Reson.*, 2012, **223**, 198–206.

63   H. Chen, A. G. Maryasov, O. Y. Rogozhnikova, D. V. Trukhin, V. M. Tormyshev and M. K. Bowman, *Phys. Chem. Chem. Phys.*, 2016, **18**, 24954–24965.

64   A. S. Lilly Thankamony, J. J. Wittmann, M. Kaushik and B. Corzilius, *Prog. Nucl. Magn. Reson. Spectrosc.*, 2017, **102–103**, 120–195.

65   P. M. L. Tammes, *Recl. des Trav. Bot. Neerl.*, 1930, **27**, 1–84.

66   T. Sugimoto and M. Tanemura, *Forma*, 2007, 157–175.

67   T. Erber and G. M. Hockney, *J. Phys. A Math. Gen.*, 1991, **24**, L1369–L1377.

68   M. Srivastava and J. H. Freed, *J. Phys. Chem. Lett.*, 2017, 5648–5655.

69   M. Srivastava, E. R. Georgieva and J. H. Freed, *J. Phys. Chem. A*, 2017, **121**, 2452–2465.

70   A. Schweiger and G. Jeschke, *Principles of Pulsed Electron Paramagnetic Resonance Spectroscopy*,

Oxford University Press, New York, 2001.

71   D. Shimon, Y. Hovav, I. Kaminker, A. Feintuch, D. Goldfarb and S. Vega, *Phys. Chem. Chem. Phys.*, 2015, **17**, 11868–11883.

72   R. I. Hunter, P. A. S. Cruickshank, D. R. Bolton, P. C. Riedi and G. M. Smith, *Phys. Chem. Chem. Phys.*, 2010, **12**, 5752–5756.